Available online at www.sciencedirect.com
ScienceDirect
Trans. Nonferrous Met. Soc. China 33(2023) 1715−1728
Transactions of Nonferrous Metals Society of China
www.tnmsc.cn

Microstructure, mechanical properties and fretting corrosion wear behavior of biomedical ZK60 Mg alloy treated by laser shock peening

Gao-qi WANG, Shou-ren WANG, Xue-feng YANG, Dao-sheng WEN, Yu GUO

School of Mechanical Engineering, University of Jinan, Jinan 250022, China

Received 25 January 2022; accepted 21 April 2022

Abstract: ZK60 magnesium alloy was treated with laser shock peening (LSP) technology at different laser energy densities. Fretting corrosion wear tests were conducted on the LSP-treated and untreated magnesium alloy samples in simulated body fluid condition. The microstructure, residual stress, surface hardness, tensile strength, and corrosion resistance were also tested to analyze their relationships with fretting corrosion wear behavior. Results showed that a maximum of 73.4% reduction of the fretting corrosion wear volume can be obtained by LSP treatment. The fine grain strengthening and the strain hardening caused by dislocation and twinning, and the compressive residual stress improve the surface hardness, tensile strength, and corrosion resistance at the same time, thus reducing the fretting corrosion wear.
Key words: microstructure; mechanical properties; fretting corrosion wear; ZK60 magnesium alloy; laser shock peening

1 Introduction

Bone plate internal fixation is one of the most common and effective methods for treating fractures. Magnesium (Mg) alloys are considered for application in bone plate implant due to their biocompatible nature and mechanical properties that are similar to human bone [1,2], avoiding stress shielding effect induced by conventional stainless steel, cobalt−chromium alloy, and titanium alloy materials. Despite the advantages, apparent obstacles of the clinical application of the Mg alloys are poor corrosion and wear resistance. Mg alloys tend to corrode at a rapid rate in the human body, thereby many efforts, such as composition design and surface treatment, have been made to control the corrosion rate [3−6]. Cold spraying technology [7], hydrothermal method [8], and plasma electrolytic oxidation method [9] were usually used to protect Mg alloy from corrosion. Wear resistance is another important factor that influences the clinical performance of bone plate. Wear resistance is directly related to the mechanical properties of surface layer of bone plate. Some surface treatment technologies, such as shot peening treatment [10] and plasma electrolytic oxidation method [11], are beneficial to the surface mechanical performance. But the friction and wear behaviors, especially the fretting wear behavior of the Mg bone plate, are often overlooked in the study.

Fretting wear is a kind of cyclic micro-movement between the screw and bone plate, and between the screw and bone caused by mutual extrusion and relative motion. The fretting wear would release wear debris to tissues that cause biological complications [12,13], also it would accelerate the generation of fatigue cracks, resulting in fatigue failure of the bone plate [14]. Besides, fretting damage may cause the bone plate to decrease its mechanical properties prematurely and

Corresponding author: Shou-ren WANG, Tel: +86-15866782561, E-mail: sherman0158@tom.com
DOI: 10.1016/S1003-6326(23)66216-8

lead to aseptic loosening [15]. Therefore, fretting wear should not be ignored during rehabilitation exercise [16].

Laser shock peening (LSP) technology is an innovative and advanced non-contact surface strengthening technology that uses a high-energy pulsed laser to induce the shock wave to plastically deform the surface of metal and alloy materials [17]. As an environmentally friendly, efficient, and ultra-high strain rate surface strengthening technology, LSP can refine the surface grain size to nanometer level and can induce compressive residual stress on the surface of materials, such as Ti, Ni, Cu, Mg and their alloys [18−22]. ZHANG et al [23] demonstrated that LSP increased the hardness and yield strength of AZ31B Mg alloy. GE and XIANG [24] found that LSP was an effective surface treatment technique to decrease fatigue crack growth rate of Mg alloy. GE et al [25] and XIONG et al [26] proved that stress corrosion resistance of AZ31B and AZ80 Mg alloys in the simulated body fluid was significantly improved after LSP treatment. PRAVEEN et al [27] stressed the advantage of using LSP as it can significantly enhance the fatigue life of Mg alloy. Recent studies have identified LSP as potential solution to reduce and control the corrosion rate [28,29]. Further, researchers proved that LSP can improve the wear resistance in dry friction conditions [30−34].

Consequently, LSP is suitable for surface modification of Mg alloy bone plates to improve mechanical, corrosive and tribological properties. However, despite the growing attention to the LSP of Mg alloys, there are few studies on the fretting wear of Mg alloy after LSP in the application of bone plate, especially the corrosion wear effect in body fluids. The tribological behavior of a material in SBF environment is different from that in dry condition [35]. Corrosion in the body fluid environment would accelerate the wear.

This research focused on the microstructure, mechanical properties and fretting corrosion wear behavior of the medical ZK60 Mg alloy after LSP in simulated body fluid (SBF). As the mechanical and tribological properties are directly related to the microscopic morphology, the microstructure of Mg alloy after LSP was observed and characterized by TEM. The mechanical properties of the Mg alloys before and after LSP were measured. The relationships among microstructure, mechanical performances and fretting corrosion behaviors of LSP-treated Mg alloys were systematically studied.

2 Experimental

2.1 Preparation of specimens

The ZK60 Mg alloy in the experiments was produced by an extrusion technique with the following chemical composition (wt.%): Zn 6.027, Zr 0.6758, Mn 0.006, Fe 0.005, Cu 0.006, Ni 0.003, and Mg balance. The samples were cut in diameter of 24 mm and thickness of 8 mm. The surfaces of all samples were ground with 600#, 800#, 1000#, 1200#, 1500#, and 2000# SiC sandpapers successively. All samples were mechanically polished until the scratches disappeared. The samples were washed in acetone for 10 min with ultrasonic cleaning machine.

2.2 Laser shock peening process

The specimens were irradiated by the Nd:YAG laser shock peening system (LSP, YS80−R200B, Xi'an Tyrida Co., Ltd., China) with a wavelength of 1064 nm. The maximum output energy of the equipment was 8 J, the pulse width was 20 ns, and the maximum processing frequency was 4 Hz. According to previous studies, energy is the most important parameter that affects the mechanical properties. Based on several preliminary experiments, the minimum laser energy that can induce plastic deformation was about 2.6 J. Moreover, samples treated with laser energy of near 8 J had no significant influence on the hardness and strength compared with 7 J samples. Therefore, four groups of specimens were prepared: (1) untreated, (2) treated with 3 J laser, (3) treated with 5 J laser, and (4) treated with 7 J laser. The overlap rate was chosen as 50%. A black tape served as protective layer was stuck on the surface of the specimens to keep the surface from heat damage caused by high temperature plasma. The surface of black tape was covered by water flow with a thickness of about 1 mm, which was served as confining layer to restrict the propagation of high pressure and temperature plasma produced by the protective layer vaporized and to enhance the peak pressure of stress wave [25]. The schematic diagrams of the LSP are shown in Fig. 1.

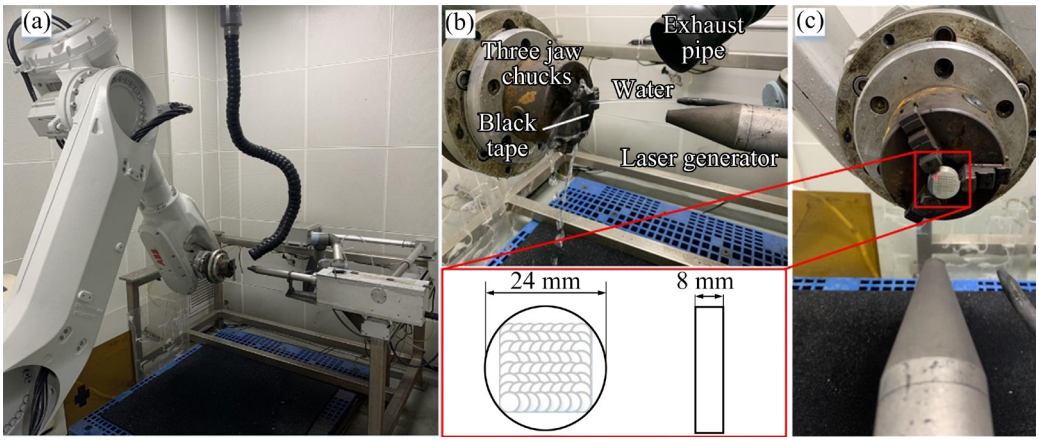

Fig. 1 Schematic diagrams of LSP: (a) LSP equipment; (b, c) LSP processing

2.3 Microstructure examination

The observation of surface microstructure was conducted using high-resolution transmission electron microscope (HRTEM, JEM−2100, Japan Electronics Co., Ltd.), operated at an acceleration voltage of 200 kV. Initially, the sample was cut into slices with dimensions of 10 mm × 10 mm × 0.5 mm using electrical discharge machining technology. Then, the slice was thinned to a thickness of about 140 μm by manual grinding. Hereafter, the flake was stamped into a wafer with a diameter of 3 mm. Subsequently, the non-reinforced surface was polished by electrolytic dual-spray thinner (MTP−1A, Jiaoda Co., Ltd., China) in a mixed solution of 97 vol.% alcohol and 3 vol.% perchloric acid at −40 °C for about 2 min. Finally, the double-sided argon-ion electrolytic polishing method was adopted to reduce the thickness of the wafer to about 60 μm.

2.4 Residual stress detection

An X-ray stress analyzer (LXRD, Proto Manufacturing Ltd., Canada) was used to measure the residual stress variation with depth. The Cr target K_α radiation was chosen with tube voltage of 30 kV and current of 20 mA. The collimating tube diameter was 1 mm, and the diffraction crystal plane was Mg(104). The samples were corroded with a Proto−8818 electrolytic polishing machine after each group of measurements. The electrolyte was saturated NaCl solution, and the corrosion depth was measured with a digital micrometer. At each depth, measurements were conducted on five randomly chosen points.

2.5 Mechanical property test

The surface hardness of untreated and LSP-treated Mg alloys was measured by a Vickers microhardness tester (402MVD, Wilson Ltd., USA) with a load of 100 g and dwell time of 15 s. Five samples were tested in each group. The mechanical properties of the specimens were measured by a universal material testing machine (Z600, ZwickRoell Co., Ltd., Germany) with strain rate of 0.02 s^{-1} at room temperature. The standard tensile specimen was cut along the longitudinal direction of the rodlike billets according to the dimensions shown in Fig. 2 using spark discharge machining. Five samples were tested in each group, and the mean values of tensile strength and elongation at break were calculated. A scanning electron microscope (SEM, JSM−7610F, Japan Electronics Co., Ltd.) was used to observe the fracture topography.

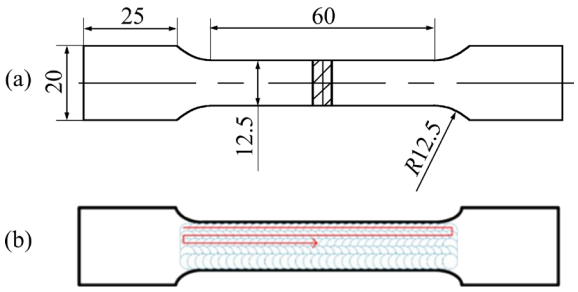

Fig. 2 Schematic diagrams of standard tensile specimen (a) and LSP processing path (b) (unit: mm)

2.6 Corrosion experiment

Corrosion resistance was evaluated by immersing experiment. The untreated and LSP-treated specimens were cut into blocks with sizes of

10 mm × 10 mm × 10 mm. The untested surfaces were covered with silica gel and immersed in SBF (Xi'an Hutt Biotechnology Co., Ltd., China), which has a pH value of 7.4−7.5. The chemical compositions of the SBF are listed in Table 1. The SBF was placed in water box with a constant temperature of (37±0.1) °C and was changed every 2 d to keep fresh. After immersion for 10 d, the specimens were ultrasonically cleaned in deionized water and dried in a drying oven. An electronic balance was employed to measure the mass loss. The corrosion rate was calculated by the mass loss and corrosion time.

Table 1 Composition of SBF (mmol/L)

Na^+	K^+	Mg^{2+}	Ca^{2+}	Cl^-	HCO_3^-	HPO_4^{2-}	SO_4^{2-}
142	5.0	1.5	2.5	103.0	10.0	1.0	0.5

2.7 Fretting wear experiment

The reciprocated sliding fretting tests were performed in SBF at (37±0.1) °C with the ball-on-disk contact configuration using fretting friction and wear testing machine (RTEC MFT−5000, RTEC Co., Ltd., USA). The schematic diagram of the fretting friction and wear tester is shown in Fig. 3. The test had a normal force of 100 N, a displacement amplitude of 100 μm, a fretting frequency of 2 Hz, and a test time of 1 h. Correspondingly, the number of cycles was 7200. The GCr15 ball (Roughness R_a was 0.02 μm, and Vickers hardness was HV 750) with a diameter of 10 mm was chosen as the counterpart. Ultrasonic cleaning was performed with acetone for 10 min after fretting wear tests. Wear volume and wear morphology were obtained by a white light interferometer (USP-Sigma, RTEC Co., Ltd., USA) and SEM. The test of each group of specimens was repeated three times.

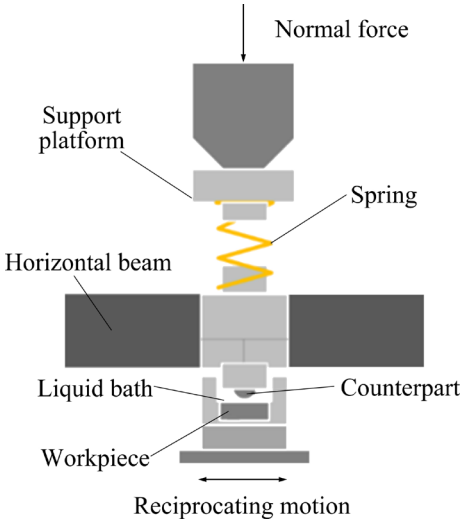

Fig. 3 Schematic diagram of fretting friction and wear test

3 Results and discussion

3.1 Microstructure

Figure 4 shows TEM images of surface microstructure of a 7 J sample under different magnifications. Figure 5 presents TEM images of the cross-section of Mg alloy near the surface and 200 μm depth away from the surface after being treated with 7 J laser. It can be known from Figs. 4(a) and (b), high angle nanoscale crystals (3−10 nm) were formed in the surface layer after LSP, illustrating that grain refinement was induced by LSP treatment. But the boundaries of some nanocrystals were not very clear due to high density dislocation accumulation caused by high-energy laser shock. The SAED pattern showed that multiple concentric circular diffraction rings were established, indicating that the degree of grain refinement was relatively high, and the nanocrystals had random crystallographic orientations [36]. It is well accepted that grain refinement has an effect of surface hardening, which can improve strength and surface hardness of metallic materials [18−20].

In addition to grain refinement, the plastic strain-induced microstructure evolution, including a great amount of dislocation and twins, was observed in the surface layer. According to Figs. 4(c) and (d), high-density and non-uniform dislocation packing and dislocation tangles were formed inside the grains of the surface layer. The dislocation tangles increased and arranged to create many dislocation walls. The uneven distribution of laser energy and the overlap of laser spots resulted in different degrees of plastic deformation in various zones. After the high-density accumulation of dislocations, boundary lines with multiple crystal grains were formed.

It can also be observed from TEM images of cross-section that there were many high-density dislocations and deformation twins near the specimen's surface (Fig. 5(a)). The mechanical twin steps and the dislocations were visibly observed in Figs. 5(b, c). Figure 5(b) illustrated SAED diagram

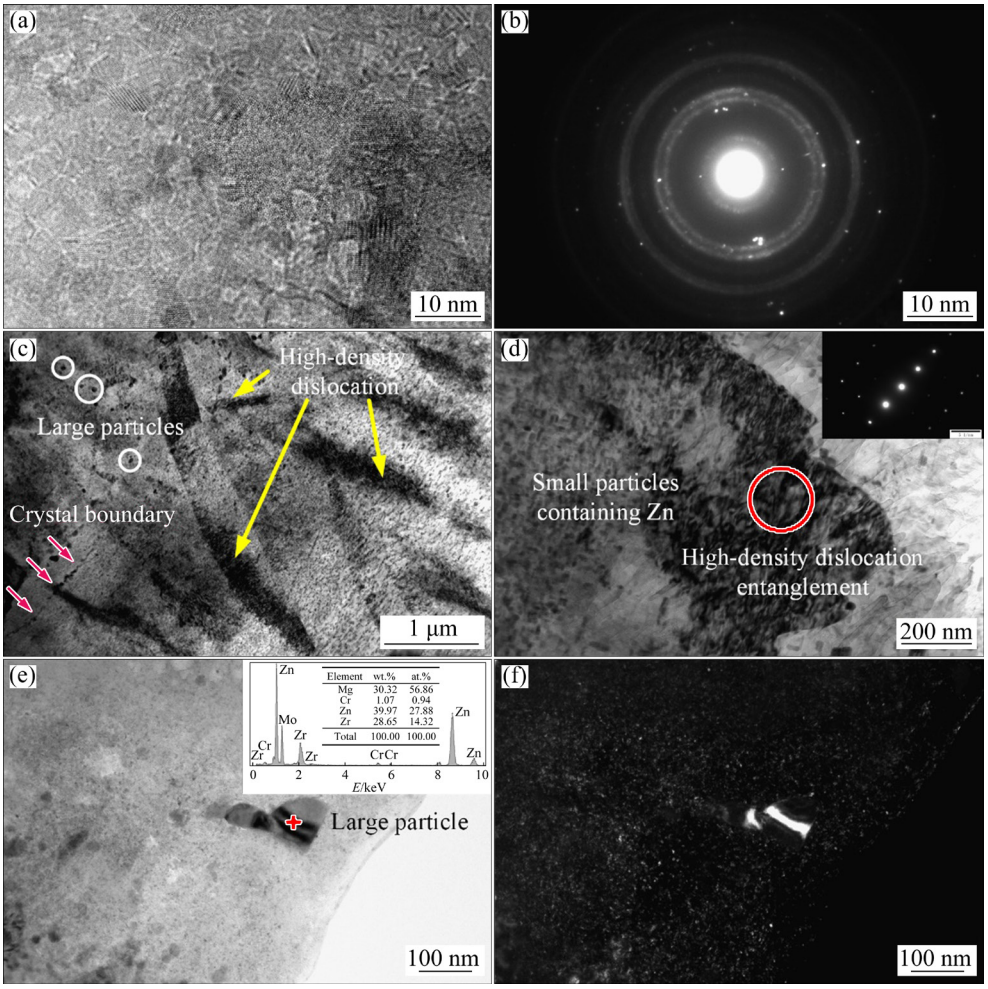

Fig. 4 TEM images of surface microstructure of 7 J sample: (a) High resolution image; (b) SAED pattern; (c) Surface deformation structure; (d) Magnified image and SAED pattern of dislocation in (c); (e) Bright field image and EDS results of second phase particles; (f) Dark field image of second phase particles

of twins, matrix, and boundaries between the twins and matrix. The positions of (100) and (102) crystal planes of twins and matrix were switched. The high-resolution images of the twin steps showed that the angle between the direction of twin texture and the substrate texture was about 90°, and the distance between fringes was about 0.55 nm, which matched well with the space between the (101) and (102) crystal planes (Fig. 5(d)). There were obvious dislocation rearrangement and annihilation at the boundaries to form nano-crystalline boundaries with high angles (Fig. 5(d)). Therefore, after LSP treatment of the Mg alloy, surface hardening effect will be realized by the synergistic effect of grain refinement and strain hardening induced by dislocation and twinning.

Bright field TEM images of the matrix about 200 μm depth away from the surface showed that there were hardly any high-density dislocations and twins (Fig. 5(e)). The SAED pattern of the matrix in Fig. 5(e) revealed that there were no nanoscale crystals in this section, and the crystallographic orientation did not show random direction. These indicated that the energy was not enough for Mg alloy to start dislocation sliding and twinning in a 200 μm depth. The laser energy degraded along the depth direction of the samples, therefore, the further away from the surface, less effect of laser shock will be received.

Besides, it can be seen from the microstructure and EDS results on the LSP-treated surface (Figs. 4(e, f)) that a large number of the second phase $MgZn_2$ particles were dispersed in the dislocation structure. The second phase particles of $MgZn_2$ were also detected to be uniformly distributed in the matrix far from the LSP-affected

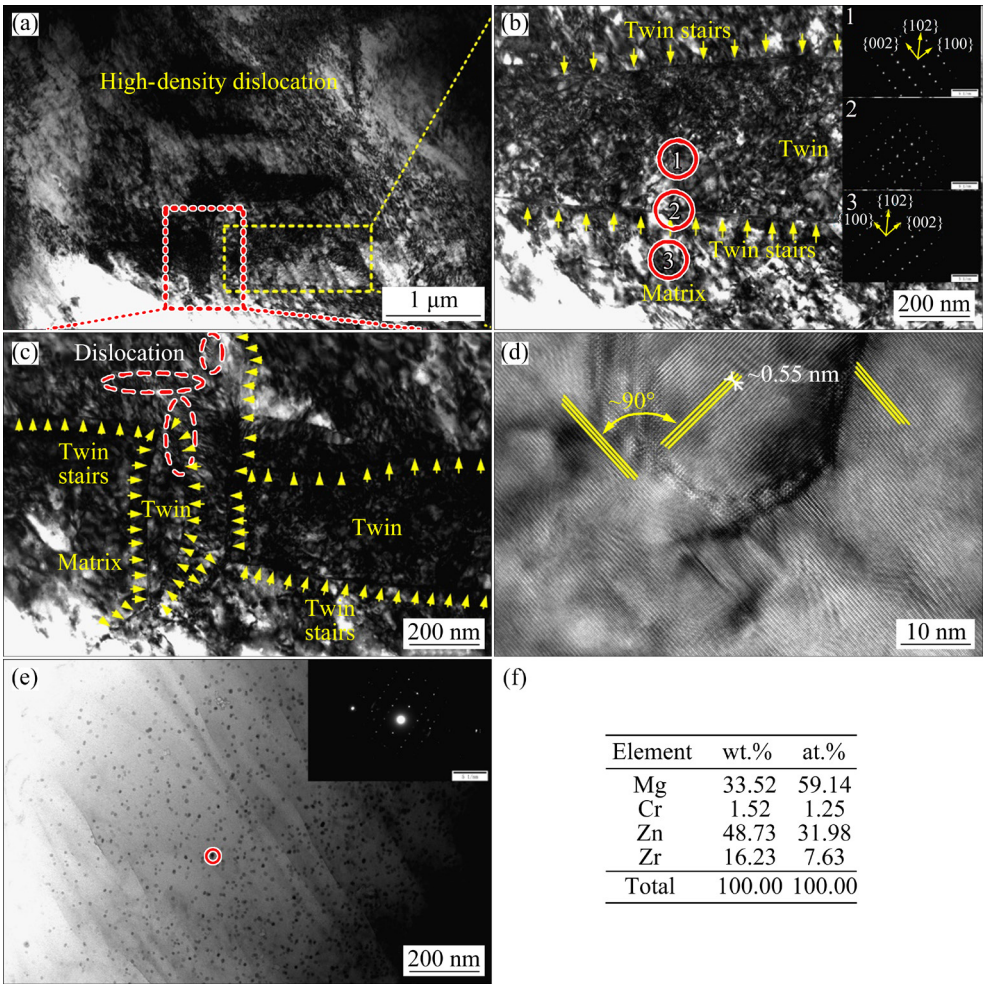

Element	wt.%	at.%
Mg	33.52	59.14
Cr	1.52	1.25
Zn	48.73	31.98
Zr	16.23	7.63
Total	100.00	100.00

Fig. 5 TEM images of cross-section microstructure of 7 J sample: (a) Microstructure near surface; (b, c) Partially enlarged view of (a); (d) High resolution image of (b); (e) TEM image at 200 μm from surface and SAED pattern with second phase particles and matrix; (f) EDS results for second phase particles in red circle of (e)

plastic deformation section (Figs. 5(e, f)), which indicated that the second phase was not produced by LSP, but existed in the original Mg alloy. LSP is a pure cold work process that causes plastic deformation and changes microstructure by mechanical force [21−24]. In spite of this, the second phase particles in the Mg alloy had enhancement effect on the dislocation strengthening induced by LSP because the particles hindered the dislocation motion, leading to higher strain hardening.

3.2 Residual stress

The mean value and standard deviation (SD) of residual stresses along the depth of the four groups of specimens are shown in Fig. 6. The residual stresses of the untreated Mg alloy were between −10 and 10 MPa. The residual stress on the surface of samples treated with 3, 5 and 7 J laser power reached −82.2, −95.3, and −106.1 MPa, respectively. With the increase of laser power, the residual compressive stress on the surface showed

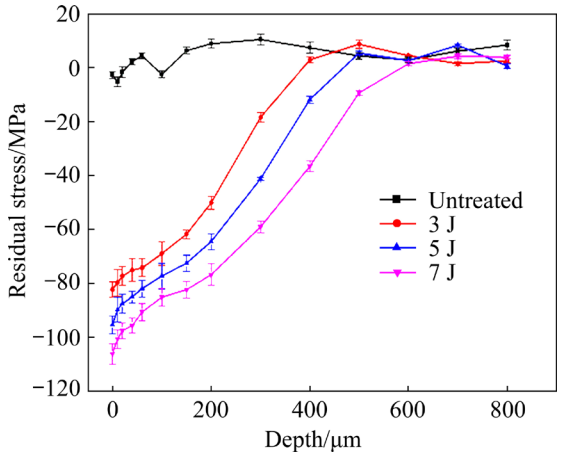

Fig. 6 Residual compressive stress along depth

an increasing trend. As the depth increased, the absolute value of compressive residual stress gradually decreased, and the depth of the influence layer of compressive residual stress of the LSP-treated samples reached to about 400, 500, and 600 μm, respectively. Similar results have been reported on Mg−3Al−1Zn alloy [31] and AZ31B magnesium alloy [24], and so on. There was obvious plastic deformation (Figs. 4 and 5) after LSP, and the dislocation entanglement and twinning caused the lattice distortion to generate a remarkable stress concentration, which led to the formation of compressive residual stress field.

3.3 Mechanical properties and fracture morphology analysis

Figure 7 illustrates that the surface hardness of Mg alloy was obviously enhanced after LSP treatment, and had positive correlation with laser power. A maximum increase of 46.6% was obtained on 7 J specimens. Figure 8 presents the tensile strength and fracture elongation of the specimens. The Mg alloy strengthened by LSP was improved in tensile strength compared with untreated samples. The tensile strength was increased by a maximum value of 13.6% after 7 J LSP treatment. However, the fracture elongation of the LSP-treated sample became smaller, which was related to the hardening effect [37].

Figure 9 shows a typical comparison of stress−strain curves of untreated and 7 J LSP-treated. It can be seen that the samples after LSP treatment have experienced the elastic deformation stage, the yield stage and the necking stage. As shown in Fig. 10, there are conspicuous differences in fracture morphology between untreated and LSP-treated samples. The original sample was characterized by large dimples, cleavage surfaces and herringbone tear ridges. Whereas, vast smaller equiaxed dimples, river-like cleavage surfaces and herringbone tear ridges were the dominating characteristics of LSP-treated Mg alloy. The fracture

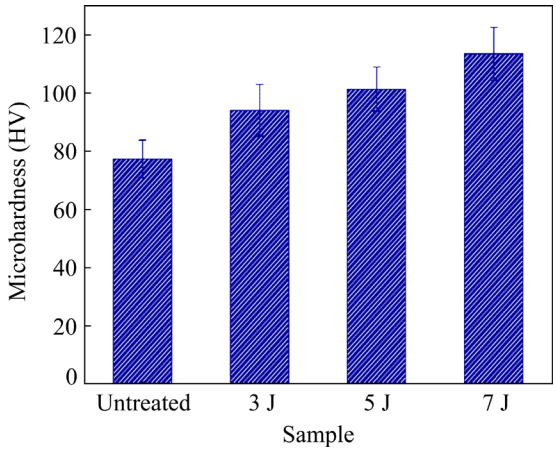

Fig. 7 Surface hardness of untreated and LSP-treated Mg alloys

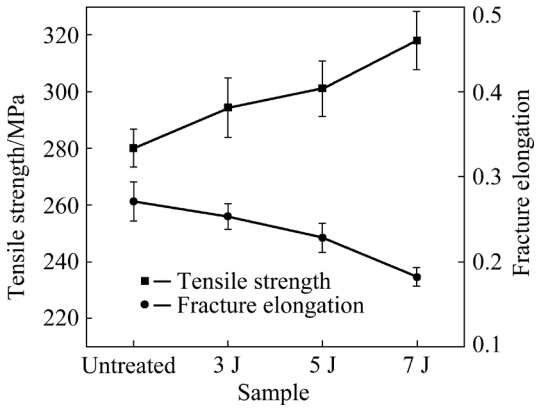

Fig. 8 Tensile strength and fracture elongation of untreated and LSP-treated samples

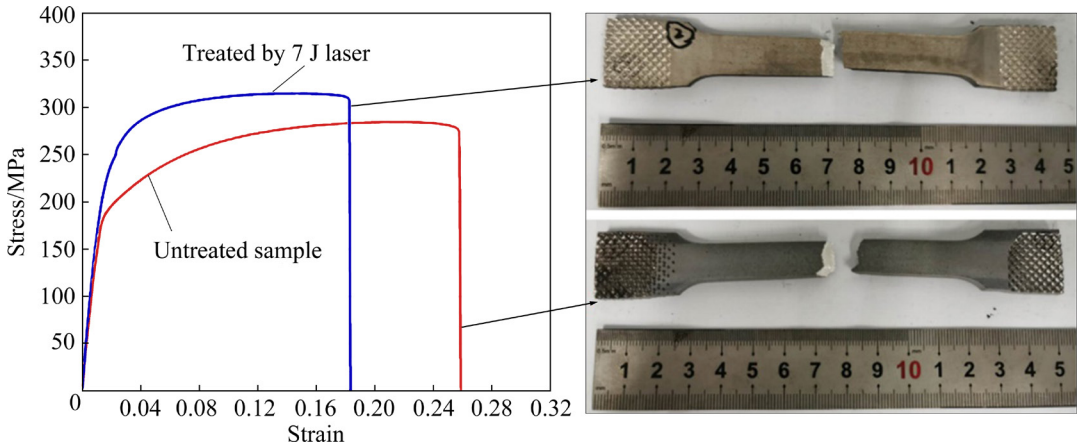

Fig. 9 Stress−strain curves of untreated and 7 J LSP-treated samples

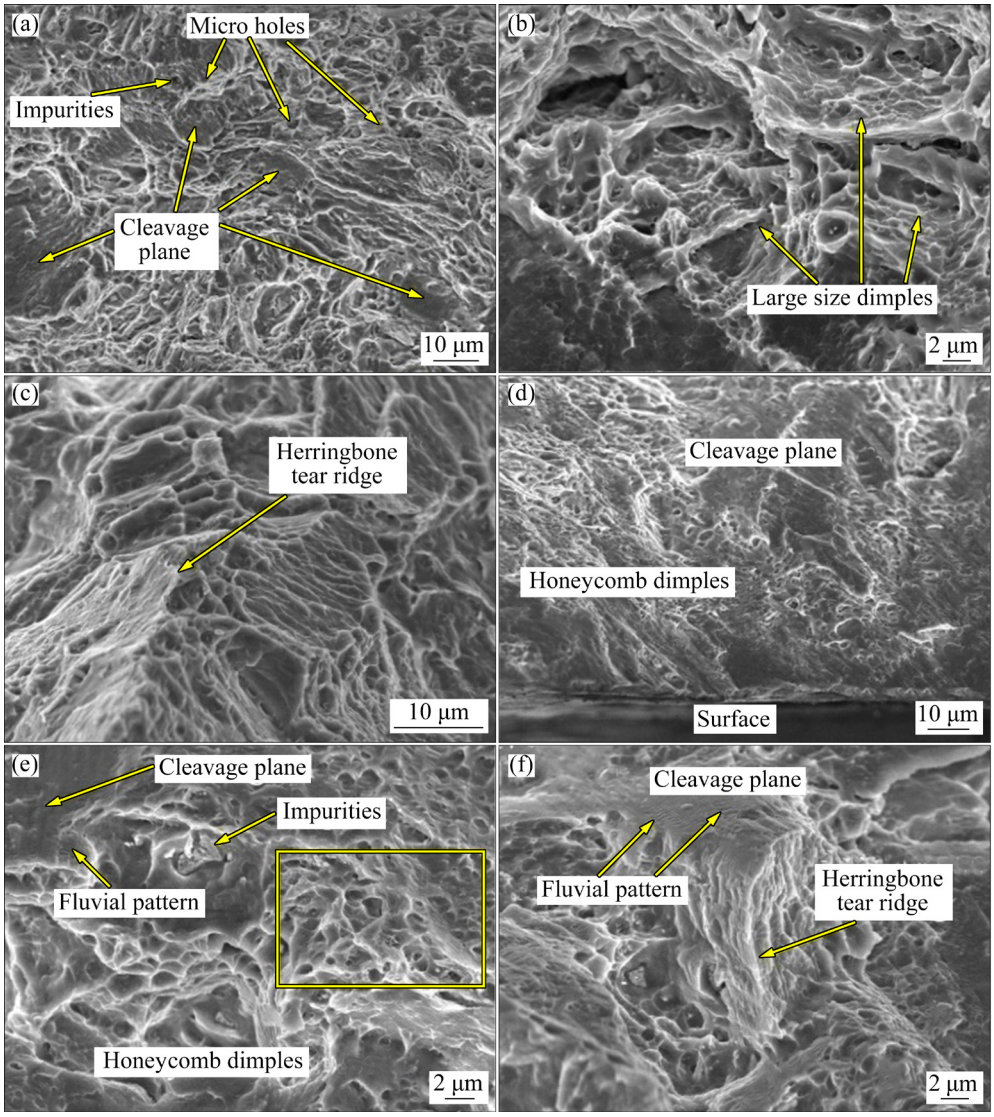

Fig. 10 SEM images of tensile fracture samples: (a−c) Untreated sample; (d−f) 7 J LSP-treated sample

modes of both samples were mixed ductile and brittle fracture.

The mechanical properties of the Mg alloy are closely related to the change of microstructure. According to the Hall−Petch formula:

$$\sigma = \sigma_0 + kd^{-1/2}$$

where σ is yield strength, σ_0 is friction stress, k is strength coefficient, and d is grain size. When the crystal grain size of metal or alloy decreases its yield strength will be higher. It can be known from Figs. 4 and 5 that LSP successfully induced the nano-crystallization of the Mg alloy. The number of grain boundaries increased after grain refinement. Most of the grain boundaries presented high angles, and the deformation of each grain would be affected by the surrounding grains. Hence, the grains were restrained by each other, and there were more impurity atoms at the grain boundaries, which would increase the retarding effect of dislocation slip. The nanocrystals with random directions and angles caused by LSP consumed the energy that is required for microcrack propagation during the stretching process, thereby delaying the generation of cracks. Simultaneously, the second phase $MgZn_2$ dispersed in the Mg alloy hindered the continuous occurrence of plastic deformation, which increased the resistance to grain boundary deformation. In addition, residual stresses played a significant role in the mechanical performance of the materials [38−40]. The high compressive residual stresses induced compression on interatomic spacing, which needed large force to break the bonds. Therefore, the surface hardness and tensile

strength of the Mg alloy subjected to LSP were improved.

Dimple size is normally influenced by the plastic deformation ability of the material, size of microvoids, plastic deformation of microvoids, and inclusions. Significant work hardening occurred after LSP [30], thus the surface hardness was greatly increased, but ductility was reduced, which was one important reason for the reduction of dimple size. On the other side, LSP produced grain refinement layer, in which the number of grain boundaries and holes increased significantly, thus increasing the number of starting points for forming dimples.

3.4 Corrosion behavior

The average corrosion rate of the specimens after the immersion in SBF for 10 d is presented in Fig. 11. The corrosion rate of the Mg alloy was obviously reduced after LSP treatment. A maximum reduction of 56.2% was shown for 7 J sample compared with untreated samples. With the increase of laser power, the corrosion rate showed a slight decreasing trend. Figure 12 shows the surface morphologies of specimens experienced corrosion for 10 d. There were large and deep etch pits and dense microcracks on the untreated Mg alloy specimen. However, the laser-treated specimens showed smaller and shallower etch pits and less microcracks. According to EDS analysis results in Table 2, magnesium oxide was the primary corrosion products. Compared with untreated specimen, the LSP-treated specimens had lower content of Mg element, but had higher contents of Ca and P elements, which were deposited from SBF, indicating that the corrosion product of magnesium was reduced after LSP treatment. The results proved that LSP treatment can improve the corrosion resistance of ZK60 Mg alloy.

The improvement of corrosion resistance after LSP treatment was mainly due to the surface

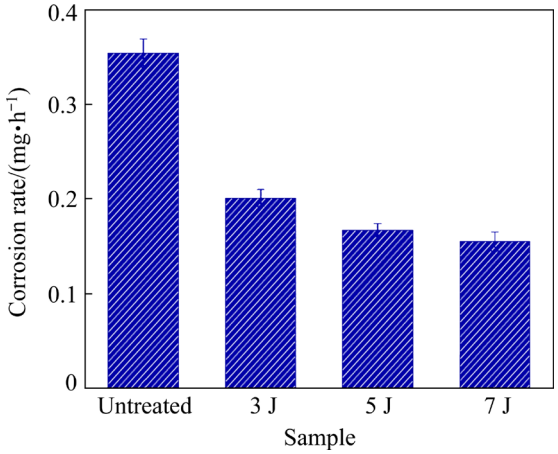

Fig. 11 Average corrosion rate of untreated and LSP-treated samples

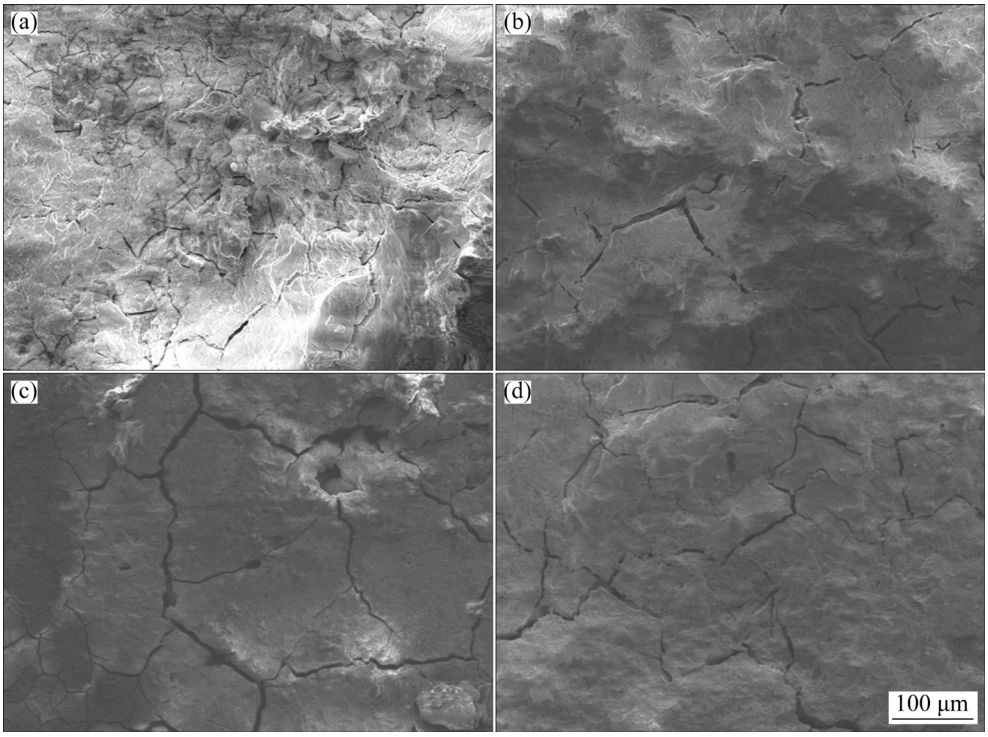

Fig. 12 Surface morphologies of specimens after corrosion for 10 d: (a) Untreated; (b) 3 J; (c) 5 J; (d) 7 J

Table 2 Element contents (wt.%) and SD (%) of specimens obtained by EDS

Element	Untreated	3 J	5 J	7 J
O	48.78 (2.41)	44.73 (1.91)	44.68 (1.26)	46.04 (0.90)
Mg	21.24 (3.37)	9.59 (0.75)	9.51 (0.52)	13.42 (2.31)
P	8.99 (2.54)	14.30 (2.40)	13.93 (1.46)	11.29 (1.00)
Ca	4.17 (1.73)	11.15 (0.37)	10.91 (2.24)	9.91 (2.74)
Zn	15.3 (1.48)	18.61 (1.23)	18.87 (1.72)	17.07 (3.12)

Data in brackets represent SD values

microstructure change and residual stress state. The refinement of surface grain produced more grain boundaries that can act as corrosion shielding. Moreover, the compressive residual stress on the surface of LSP-treated specimens made the surface grains and passivation film denser, and had the effect of preventing crack initiation and extension, thus increasing the corrosion resistance.

3.5 Fretting corrosion wear behavior

Figure 13 shows the friction coefficient and wear volume of each sample in the SBF lubrication state. The friction coefficient slightly decreased with the increase of laser energy. The wear volume presented significant reduction as the laser energy increased, and the maximum wear volume was reduced by 73.4% after LSP. Figure 14 illustrates the wear scar and the wear depth, which showed a similar trend with wear volume. The above results indicate that the fretting wear resistance of the Mg alloys is significantly improved after being strengthened by higher laser energy.

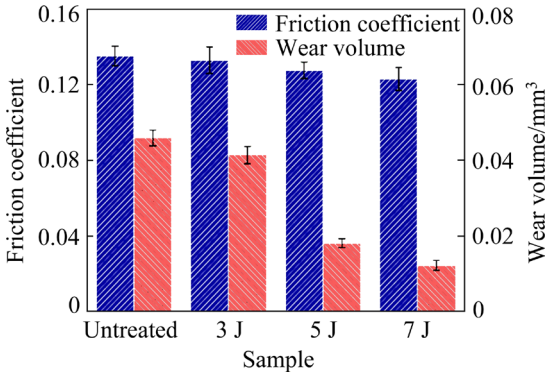

Fig. 13 Friction coefficient and wear volume of untreated and LSP-treated samples

Figure 15 shows the micrographs of wear scars of the samples. The locally enlarged view of Figs. 15(a_1, a_2) indicated that there were many white corrosion products and corrosion pores on the surface of untreated samples. The proportion of corrosion pores was relatively large in the whole wear mark. In the SBF solution, the Mg alloy reacted with water to form $Mg(OH)_2$. The Cl^- in the SBF solution converted $Mg(OH)_2$ into more soluble $MgCl_2$, which accelerated the dissolution of the Mg alloy, making the surface loose and porous, and easy to wear [41]. In addition, there were shallow and visible furrows on the worn surface and many cracks at the bottom of corrosion pores (Fig. 15(a_3)), because the Mg alloy had lower hardness than the counterpart GCr15. The wear mechanism of untreated Mg alloy in SBF condition was a combination of corrosive wear and abrasive wear.

After 3 J and 5 J laser modification, the surface morphology was changed obviously. The corrosion area, amount of corrosion products and corrosion pores were reduced, but there were still a few cracks. For the 7 J sample, the edge of the fretting wear mark was not clear. The number of neat cracks on the substrate surface was further reduced, and no corrosion pores were found. Moreover, the furrows in LSP-treated Mg alloy were slighter than those in the untreated Mg alloy. Consequently, the wear mechanism of 7 J LSP-treated Mg alloy was mainly abrasive wear. The change of wear mode before and after LSP treatment was attributed to the enhancement of surface hardness and corrosion resistance, which has an effect of reducing abrasive wear and corrosive wear.

The improvement of the wear resistance is inseparable from the changes of the microstructure, mechanical properties and corrosion resistance. Under the environment of liquid with corrosivity, corrosion will emerge on the surface layer of the material, the combination of corrosion effect and wear effect results in significant mutual reinforcement [42,43]. LSP refines surface grains and produces a plastic deformation layer with uneven dislocations and deformation twins, causing the generation of compressive residual stress. The

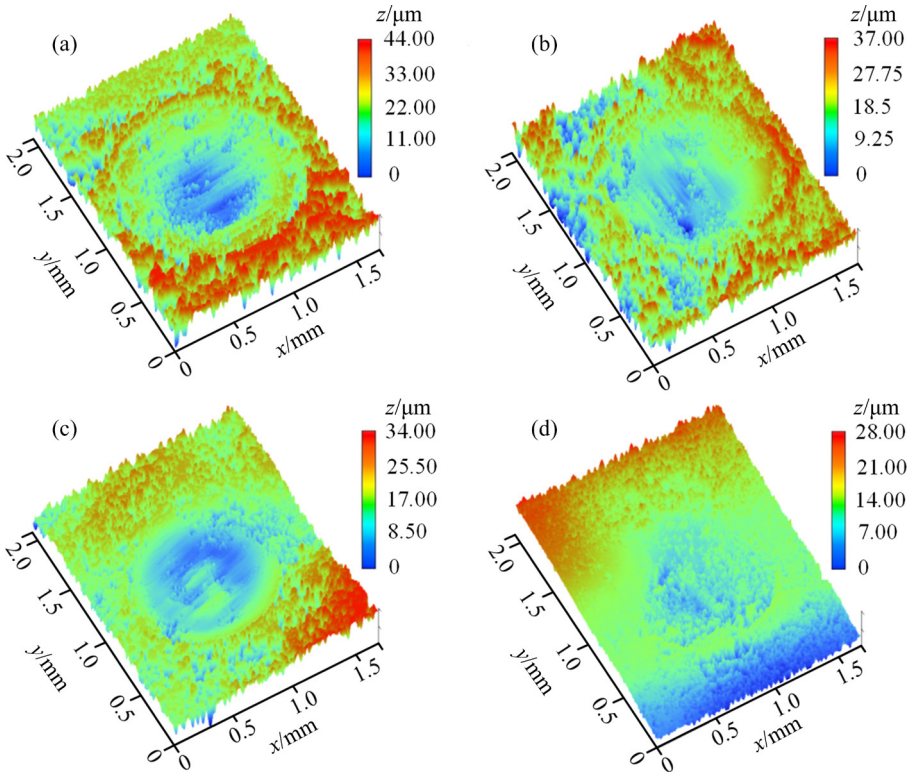

Fig. 14 3D contour maps of wear scar: (a) Untreated sample; (b) 3 J; (c) 5 J; (d) 7 J

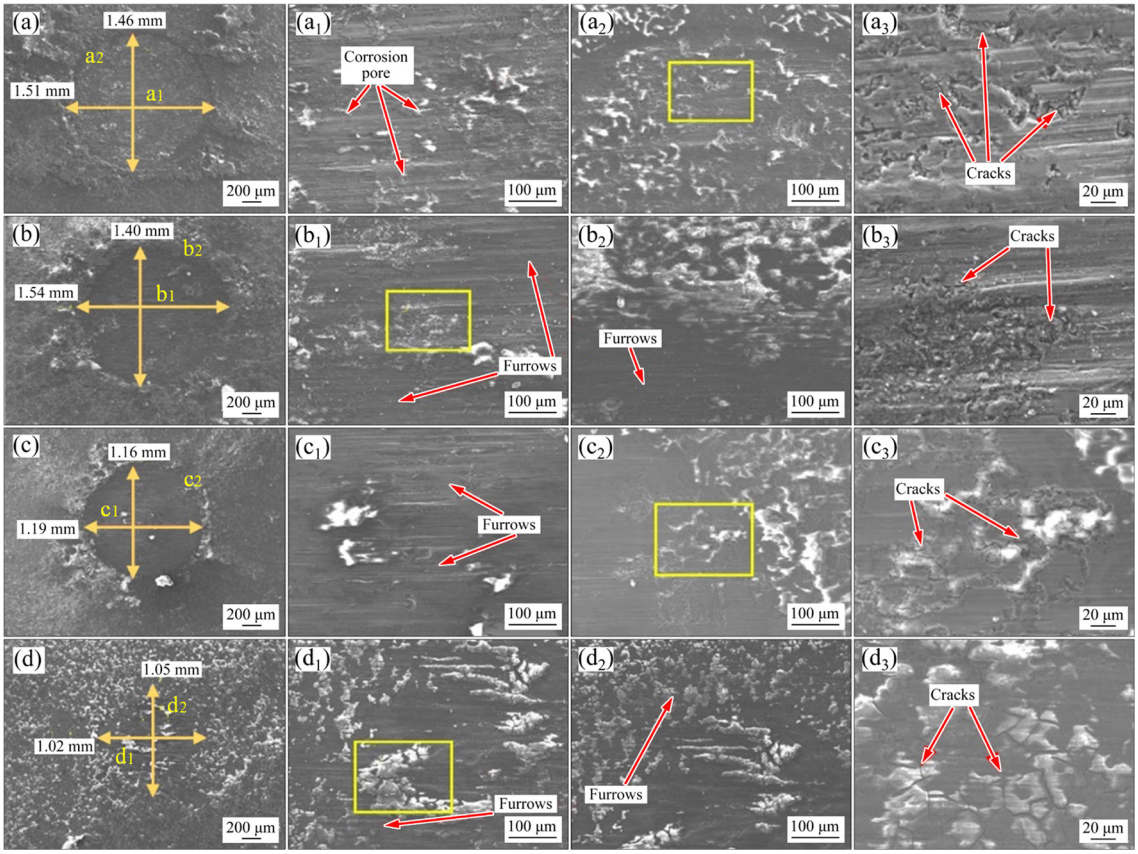

Fig. 15 Micrographs of worn surface after friction in SBF: (a, a_1−a_3) Untreated; (b, b_1−b_3) 3 J; (c, c_1−c_3) 5 J; (d, d_1−d_3) 7 J ((a_1−d_1) and (a_2−d_2) are magnified views of areas marked in (a−d), respectively; (a_3−d_3) are magnified views of the yellow rectangular areas in (a_2, b_1, c_2, d_1), respectively)

fine grain strengthening effect, the strain hardening effect, and the compressive residual stress improve the surface hardness, tensile strength and corrosion resistance simultaneously. Therefore, LSP can significantly improve the fretting corrosion resistance of Mg alloy in the SBF.

4 Conclusions

(1) LSP induces grain refinement on the surface of ZK60 Mg alloy, and the size of the nanocrystals can reach 3−10 nm. Microstructure evolution of dislocation and twinning is simultaneously induced in the Mg alloy by the high-energy laser shock. The dislocation and twinning cause the plastic deformation and lattice distortion that lead to the generation of strain hardening effect and remarkable residual compressive stress.

(2) The strain hardening, the fine grain strengthening and the compressive residual stress improve the surface hardness, tensile strength and corrosion resistance at the same time, therefore enhancing the fretting corrosion resistance of ZK60 Mg alloy in SBF. A maximum of 73.4% reduction of wear volume can be obtained by 7 J laser-treated Mg alloy compared to untreated specimen.

Acknowledgments

This work was supported by the National Natural Science Foundation of China (Nos. 51872122, 52105258), the Major Basic Research Project of Shandong Natural Science Foundation, China (No. ZR2020ZD06), the Independent Innovation Team Funding in Jinan, China (No. 2019GXRC012), the Key Projects of Shandong Natural Science Foundation, China (No. ZR2020KE062), the Taishan Scholar Engineering Special Funding, China (No. ts201511040), and the Project of Shandong Province Higher Educational Youth Innovation Science and Technology Program, China (No. 2019KJB021).

References

[1] DENKENA B, LUCAS A. Biocompatible magnesium alloys as absorbable implant materials-adjusted surface and subsurface properties by machining processes [J]. CIRP Annals, 2007, 56: 113−116.

[2] DING Wen-jiang. Opportunities and challenges for the biodegradable magnesium alloys as next-generation biomaterials [J]. Regenerative Biomaterials, 2016, 3: 79−86.

[3] BAZHENOV V E, LI A V, KOMISSAROV A A, KOLTYGIN A V, TAVOLZHANSKII S A, BAUTIN V A. Microstructure and mechanical and corrosion properties of hot-extruded Mg−Zn−Ca−(Mn) biodegradable alloys [J]. Journal of Magnesium and Alloys, 2021, 9: 1428−1442.

[4] YU Lei-ting, ZHAO Zi-han, TANG Chao-kun, LI Wei, YOU Chen, CHEN Min-fang. The mechanical and corrosion resistance of Mg−Zn−Ca−Ag alloys: The influence of Ag content [J]. Journal of Materials Research and Technology, 2020, 9: 10863−10875.

[5] LIU Bao-sheng, CAO Miao-miao, ZHANG Yue-zhong, HU Yong, GONG Chang-wei, HOU Li-feng, WEI Ying-hui. Microstructure, anticorrosion, biocompatibility and antibacterial activities of extruded Mg−Zn−Mn strengthened with Ca [J]. Transactions of Nonferrous Metals Society of China, 2021, 31: 358−370.

[6] WU Shu-xu, WANG Shou-ren, WANG Gao-qi, YU Xiu-chun, LIU Wen-tao, CHANG ZQ. Microstructure, mechanical and corrosion properties of magnesium alloy bone plate treated by high-energy shot peening [J]. Transactions of Nonferrous Metals Society of China, 2019, 29: 1641−1652.

[7] YAO Hai-long, HU Xiao-zhen, YI Zhi-hai, XIA Jing, TU Xing-yu, LI Shi-bin, YU Bo, ZHANG Meng-xian. Microstructure and improved anti-corrosion properties of cold-sprayed Zn coatings fabricated by post shot-peening process [J]. Surface and Coatings Technology, 2021, 422: 127557.

[8] SONG Zheng-wei, XIE Zhi-hui, DING Li-feng, ZHANG Yu-jing, HU Xi-yan. Preparation of corrosion-resistant MgAl-LDH/Ni composite coating on Mg alloy AZ31B [J]. Colloids and Surfaces A: Physicochemical and Engineering Aspects, 2022, 632: 127699.

[9] WEI Bing-jian, CHENG Yu-lin, LIU Yuan-yuan, ZHU Zhun-da, CHENG Ying-liang. Corrosion and wear resistance of AZ31 Mg alloy treated by duplex process of magnetron sputtering and plasma electrolytic oxidation [J]. Transactions of Nonferrous Metals Society of China, 2021, 31: 2287−2306.

[10] MENEZES M R, GODOY C, BUONO V, SCHVARTZMAN M, WILSON A B. Effect of shot peening and treatment temperature on wear and corrosion resistance of sequentially plasma treated AISI 316L steel [J]. Surface and Coatings Technology, 2017, 309: 651−662.

[11] DAVOODI D F, ATAPOUR M, BLAWERT C, ZHELUDKEVICH M. Wear and corrosion behavior of clay containing coating on AM 50 magnesium alloy produced by aluminate-based plasma electrolytic oxidation [J]. Transactions of Nonferrous Metals Society of China, 2021, 31: 3719−3738.

[12] ALVES S A, ROSSI A L, RIBEIRO A R, TOPTAN F, PINTO A M, CELIS J. Tribo-electrochemical behavior of bio-functionalized TiO_2 nanotubes in artificial saliva: Understanding of degradation mechanisms [J]. Wear, 2017, 384: 28−42.

[13] BUCIUMEANU M, ARAUJO A, CARVALHO O, MIRANDA G, SOUZA J C M, SILVA F. Study of the tribocorrosion behaviour of Ti6Al4V−HA biocomposites [J].

Tribology International, 2017, 107: 77−84.

[14] COHEN J. Corrosion testing of orthopaedic implants [J]. The Journal of Bone & Joint Surgery, 1962, 44: 307−316.

[15] KAJETANEK C, BOUYER B, OLLIVIER M, BEAUFILS P, BOISRENOULT P, PUJOL N. Mid-term survivorship of Mini-keel^{TM} versus Standard keel in total knee replacements: Differences in the rate of revision for aseptic loosening [J]. Orthopaedics & Traumatology, 2016, 102: 611−617.

[16] ZHU M H, CAI Z B, LI W, YU H Y, ZHOU Z R. Fretting in prosthetic devices related to human body [J]. Tribology International, 2009, 42: 1360−1364.

[17] SHARMA A, SONG J, FURFARI D, MANNAVA S R, VASUDEVAN V K. Remarkable near-surface microstructure of nanoparticles and oxide film in laser shock peened Al−Zn−Mg−Cu alloy [J]. Scripta Materialia, 2021, 202: 114012.

[18] MAO Bo, LIAO Yi-liang, LI Bin. Gradient twinning microstructure generated by laser shock peening in an AZ31B magnesium alloy [J]. Applied Surface Science, 2018, 457: 342−351.

[19] LU J Z, WU L J, SUN G F, LUO K Y, ZHANG Y K, CAI J. Microstructural response and grain refinement mechanism of commercially pure titanium subjected to multiple laser shock peening impacts [J]. Acta Materialia, 2017, 127: 252−266.

[20] CHEN Lan, REN Xu-dong, ZHOU Wang-fan, TONG Zhao-peng, ADU-GYAMFI S, YE Yun-xia, REN Yun-peng. Evolution of microstructure and grain refinement mechanism of pure nickel induced by laser shock peening [J]. Materials Science and Engineering A, 2018, 728: 20−29.

[21] WEI Bo-xin, XU Jin, FRANK C Y, WU Jia-jun, SUN Cheng, WANG Zheng-yao. Microstructural response and improving surface mechanical properties of pure copper subjected to laser shock peening [J]. Applied Surface Science, 2021, 564: 150336.

[22] LIU Guang-lei, CAO Yu-hao, YANG Kun, GUO Wei, SUN Xiao-xuan, ZHAO Ling, SI Nai-chao, ZHOU Jian-zhong. Thermal fatigue crack growth behavior of $ZCuAl_{10}Fe_3Mn_2$ alloy strengthened by laser shock processing [J]. Transactions of Nonferrous Metals Society of China, 2021, 31: 1023−1030.

[23] ZHANG R X, ZHOU X F, GAO H Y, MANKOCI S, LIU Y, SANG X H. The effects of laser shock peening on the mechanical properties and biomedical behavior of AZ31B magnesium alloy [J]. Surface and Coatings Technology, 2018, 339: 48−56.

[24] GE Mao-zhong, XIANG Jian-yun. Effect of laser shock peening on microstructure and fatigue crack growth rate of AZ31B magnesium alloy [J]. Journal of Alloys and Compounds, 2016, 680: 544−552.

[25] GE M Z, XIANG J Y, YANG L, WANG J T. Effect of laser shock peening on the stress corrosion cracking of AZ31B magnesium alloy in a simulated body fluid [J]. Surface and Coatings Technology, 2017, 310: 157−165.

[26] XIONG Ying, HU Xia-xia, WENG Ze-yu, SONG Ren-guo. Stress corrosion resistance of laser shock peening/microarc oxidation reconstruction layer fabricated on AZ80 magnesium alloy in simulated body fluid [J]. Journal of Materials Engineering and Performance, 2020, 29: 5750−5756.

[27] PRAVEEN T R, SHIVANANDA N H, SWAROOP S. Influence of equal channel angular pressing and laser shock peening on fatigue behaviour of AM80 alloy [J]. Surface and Coatings Technology, 2019, 369: 221−227.

[28] CARALAPATTI V K, NARAYANSWAMY S. Effect of high repetition laser shock peening on biocompatibility and corrosion resistance of magnesium [J]. Optics & Laser Technology, 2017, 88: 75−84.

[29] SHEN Yong-shui, HE Liu-yong, YANG Zeng-yuan, XIONG Ying. Corrosion behavior of different coatings prepared on the surface of AZ80 magnesium alloy in simulated body fluid [J]. Journal of Materials Engineering and Performance, 2020, 29: 1609−1621.

[30] GUO Yu, WANG Shou-ren, LIU Wen-tao, SUN Zhao-lei, ZHU Guo-dong, XIAO Teng. Effect of laser shock peening on tribological properties of magnesium alloy ZK60 [J]. Tribology International, 2020, 144: 160138.

[31] GE M Z, XIANG J Y, TANG Y, YE X, FAN Z, LU Y L. Wear behavior of Mg−3Al−1Zn alloy subjected to laser shock peening [J]. Surface and Coatings Technology, 2018, 337: 501−509.

[32] MAO B, SIDDAIAH A, ZHANG X, LI B, MENEZES P L, LIAO Y L. The influence of surface pre-twinning on the friction and wear performance of an AZ31B Mg alloy [J]. Applied Surface Science, 2019, 480: 998−1007.

[33] SIDDAIAH A, MAO B, KASAR A K, LIAO Y L, MENEZES P L. Influence of laser shock peening on the surface energy and tribocorrosion properties of an AZ31B Mg alloy [J]. Wear, 2020, 462/463: 203490.

[34] NIE Xiang-fan, ZHAO Fei-fan, TIAN Le, YAN Li. Tribology performance of laser-peened MB8 magnesium alloy under different working conditions [J]. The International Journal of Advanced Manufacturing Technology, 2021, 112: 1661−1673.

[35] WANG Gao-qi, WANG Shou-ren, YANG Xue-feng, YU Xiu-chun, WEN Dao-sheng, CHANG Zheng-qi. Fretting wear and mechanical properties of surface-nanostructural titanium alloy bone plate [J]. Surface and Coatings Technology, 2021, 405: 126512.

[36] LI Jing, ZHOU Jian-zhong, FENG Ai-xin, HUANG Yu, TIAN Xu-liang, HUANG Shu. Twin formation and its strengthening mechanism of pure titanium processed by cryogenic laser peening [J]. Optics & Laser Technology, 2019, 120: 105763.

[37] LUO K Y, WANG C Y, SUN G F, CUI C Y, SHENG J, LU J Z. Investigation and microstructural analyses of massive LSP impacts with coverage area on crack initiation location and tensile properties of AM50 magnesium alloy [J]. Materials Science and Engineering A, 2016, 650: 110−118.

[38] HUANG Y C, CHANG S Y, CHANG C H. Effect of residual stresses on mechanical properties and interface adhesion strength of SiN thin films [J]. Thin Solid Films, 2009, 517: 4857−4861.

[39] ZHOU Jian-zhong, LI Jing, HUANG Shu, SHENG Jie, MENG Xian-kai, SUN Qi, SUN Yun-hui, XU Gao-feng, SUN Yun-jie, LI Hua-ting. Influence of cryogenic treatment prior to laser peening on mechanical properties and microstructural characteristics of TC6 titanium alloy [J]. Materials Science and Engineering A, 2018, 718: 207−215.

[40] HE Z R, SHEN Y Z, TAO J, CHEN H F, ZENG X F, HUANG X, EL-ATY A A. Laser shock peening regulating aluminum alloy surface residual stresses for enhancing the mechanical properties: Roles of shock number and energy [J]. Surface and Coatings Technology, 2021, 421: 127481.
[41] LIU De-bao, WU Bo, WANG Xiao, CHEN Min-fang. Corrosion and wear behavior of an Mg−2Zn−0.2Mn alloy in simulated body fluid [J]. Rare Metals, 2015, 34(8): 553−559.
[42] WATSON S W, FRIEDERSDORF F J, MADSEN B W, CRAMER S D. Methods of measuring wear-corrosion synergism [J]. Wear, 1995, 181/182/183: 476−484.
[43] HENRY P, TAKADOUM J, BERÇOT P. Tribocorrosion of 316L stainless steel and TA6V4 alloy in H_2SO_4 media [J]. Corrosion Science, 2009, 51: 1308−1314.

激光喷丸强化 ZK60 医用镁合金的显微组织、力学性能及微动腐蚀行为

王高琦，王守仁，杨学锋，温道胜，郭 宇

济南大学 机械工程学院，济南 250022

摘 要：采用不同能量密度激光对 ZK60 镁合金进行喷丸强化处理，并对处理前后的试样进行模拟体液条件下的微动腐蚀磨损实验。测试试样的显微组织、残余应力、表面硬度、抗拉强度和耐腐蚀性，并分析其与微动腐蚀磨损行为的关系。结果表明，激光喷丸强化处理可使镁合金的微动腐蚀磨损体积降低 73.4%。位错和孪晶引起的细晶强化作用和应变强化作用以及残余压应力提高了镁合金表面硬度、抗拉强度和耐腐蚀性，因而降低了微动腐蚀磨损。

关键词：显微组织；力学性能；微动腐蚀磨损；ZK60 镁合金；激光喷丸强化

(Edited by Wei-ping CHEN)